JVST A Journal of Vacuum Science & Technology A

Plasmonic nanocomposites of zinc oxide and titanium nitride

Cite as: J. Vac. Sci. Technol. A **38**, 042404 (2020); https://doi.org/10.1116/1.5142858
Submitted: 17 December 2019 . Accepted: 13 May 2020 . Published Online: 02 June 2020

Chad A. Beaudette, Jacob T. Held, Benjamin L. Greenberg, Phong H. Nguyen, Nolan M. Concannon, Russell J. Holmes, K. Andre Mkhoyan, Eray S. Aydil, and Uwe R. Kortshagen

COLLECTIONS

Paper published as part of the special topic on Atomic Layer Deposition (ALD)
Note: This paper is part of the 2021 Special Topic Collection on Atomic Layer Deposition (ALD).

ARTICLES YOU MAY BE INTERESTED IN

Comprehensive characterization of copper oxide atomic layer deposition using water or ozone with enhanced bis-(dimethylamino-2-propoxide) copper delivery
Journal of Vacuum Science & Technology A **38**, 042403 (2020); https://doi.org/10.1116/6.0000248

Inside the mysterious world of plasma: A process engineer's perspective
Journal of Vacuum Science & Technology A **38**, 031004 (2020); https://doi.org/10.1116/1.5141863

The role of plasma in plasma-enhanced atomic layer deposition of crystalline films
Journal of Vacuum Science & Technology A **38**, 040801 (2020); https://doi.org/10.1116/6.0000145

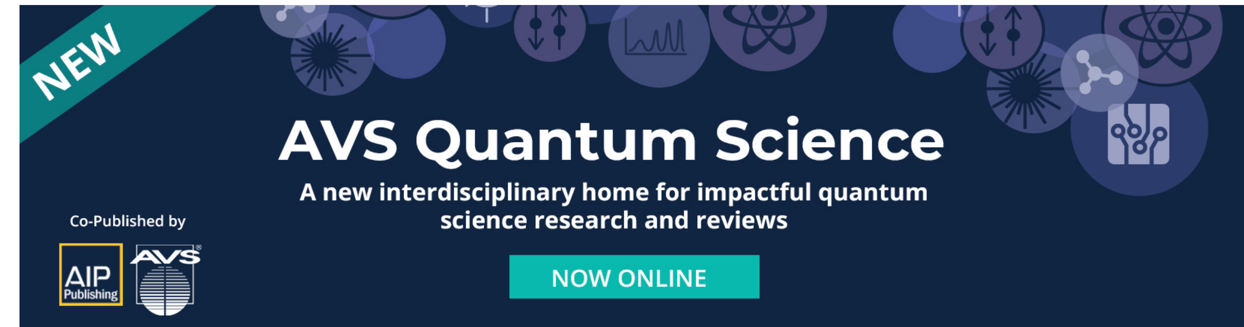

© 2020 Author(s).

JVST A
Journal of Vacuum Science & Technology A

ARTICLE

avs.scitation.org/journal/jva

Plasmonic nanocomposites of zinc oxide and titanium nitride

Cite as: J. Vac. Sci. Technol. A **38**, 042404 (2020); doi: 10.1116/1.5142858
Submitted: 17 December 2019 · Accepted: 13 May 2020 ·
Published Online: 2 June 2020

View Online
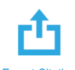
Export Citation

CrossMark

Chad A. Beaudette,[1,a)] Jacob T. Held,[2,b)] Benjamin L. Greenberg,[1,c)] Phong H. Nguyen,[3,d)] Nolan M. Concannon,[2,e)] Russell J. Holmes,[2,f)] K. Andre Mkhoyan,[2,g)] Eray S. Aydil,[2,4,h)] and Uwe R. Kortshagen[1,a)]

AFFILIATIONS

[1]Department of Mechanical Engineering, University of Minnesota, Minneapolis, Minnesota 55455
[2]Department of Chemical Engineering and Materials Science, University of Minnesota, Minneapolis, Minnesota 55455
[3]Department of Biomedical, Biological & Chemical Engineering, University of Missouri, Columbia, Missouri 65211
[4]Department of Chemical and Biomolecular Engineering, Tandon School of Engineering, Brooklyn, New York 11201

Note: This paper is part of the 2021 Special Topic Collection on Atomic Layer Deposition (ALD).

[a)]**Authors to whom correspondence should be addressed:** beaud076@umn.edu and kortshagen@umn.edu
[b)]**Electronic mail:** heldx123@umn.edu
[c)]**Electronic mail:** bengreenberg@umn.edu
[d)]**Electronic mail:** phong.nguyen@mail.missouri.edu
[e)]**Electronic mail:** conca014@umn.edu
[f)]**Electronic mail:** rholmes@umn.edu
[g)]**Electronic mail:** aydil@nyu.edu
[h)]**Electronic mail:** mkhoyan@umn.edu

ABSTRACT

The authors produce plasmonic ZnO-TiN nanocomposite films by depositing plasma-synthesized ZnO nanocrystals onto a substrate and then by infilling the nanocrystal network's pores with TiN via remote plasma-enhanced atomic layer deposition (PEALD). This ZnO-TiN nanocomposite exhibits a plasmonic resonance that is blueshifted compared to planar titanium nitride thin films. The authors study the effects of PEALD conditions and the ZnO film thickness on the plasmonic response of these nanocomposites and exploit the optimized film in a device that generates photocurrent at zero bias.

Published under license by AVS. https://doi.org/10.1116/1.5142858

I. INTRODUCTION

Nanocrystal (NC)-based nanocomposites are typically formed by first depositing a NC film from the liquid or gas phase and subsequently filling the voids in the NC network via atomic layer deposition (ALD).[1–6] Such nanocomposites have been shown to be robust and stable under ambient conditions with improved electrical and optical performance as compared to films without infilling.[2,3] In particular, NC-based nanocomposites that combine semiconductors with plasmonic materials offer intriguing platforms for optoelectronic devices, including devices that exploit hot electrons for current generation. New combinations of semiconducting and plasmonic materials may be enabled by using plasma-enhanced atomic layer deposition (PEALD) rather than conventional thermal ALD to infill NC networks. Currently, PEALD is used relatively rarely for infilling tortuous NC networks. However, in principle, developing this technique may enable the production of nanocomposites with compositions and properties unobtainable via thermal ALD.

Here, we explore nanocomposites of zinc oxide (ZnO) and titanium nitride (TiN). TiN has attractive plasmonic properties and can be produced by a variety of deposition methods. Its plasmonic response in the near infrared[7] has found uses in optoelectronic devices,[8,9] photothermal therapy,[10] IR selective coatings,[11] sensing,[12,13] waveguides,[14] diffusion barriers,[15] and photocatalysis.[16–18] Experimentally realized plasmonic TiN

Published under license by AVS.

nanostructures include nanorods,[13,19] semishells,[7] nanoparticles,[20–22] nanotubes and nanohills,[23] and gratings.[24] A variety of TiN deposition and synthesis methods are available, including plasma-enhanced chemical vapor deposition,[25] magnetron sputtering,[23,26] nonthermal plasma synthesis,[21,22] aerosol synthesis,[27] and colloidal synthesis.[28] However, these methods are ill-suited for conformally infilling the pores in NC networks to produce dense nanocomposites. For this application, ALD and PEALD are excellent candidates.

ALD, which is typically employed for conformally coating high aspect ratio features in semiconductor processing,[2,4,6,29,30] is a well-suited approach to infilling NC networks, especially with an amorphous material.[1,2,4–6] However, thermal ALD of crystalline plasmonic TiN requires high deposition temperatures, 500 °C or greater, or an even higher-temperature postanneal.[31–33] Consequently, low-temperature TiN ALD has typically been used in nonplasmonic applications.[34,35] Successful examples of TiN ALD utilized tetrakis(dimethylamido)titanium(IV) (TDMAT)[32,34–38] or titanium tetrachloride ($TiCl_4$)[31,33] with reactive ammonia (NH_3) as a coreactant.

To circumvent the limited reactivity of some ALD precursors at low temperature, nonthermal plasmas are used in PEALD to produce radicals and metastable species. Because the plasma in PEALD produces nitrogen radicals through high-energy electron impact rather than relying on chemical reactions, PEALD approaches can often utilize safer, lower-reactivity gases, such as N_2 instead of NH_3. Reports of successful synthesis of low-impurity TiN via PEALD have employed TDMAT as the titanium source with an NH_3 (Refs. 37–40) or an N_2 (Refs. 26, 36, 39, and 41–44) plasma. Other coreactants such an H_2 (Refs. 45–47) plasma have been used, but these films often have a significant quantity of carbon impurities. Some have also used $TiCl_4$ with an NH_3 (Refs. 48 and 49) or an N_2 (Ref. 50) plasma as the coreactant. TDMAT is an attractive precursor because its reactions with nitrogen can produce TiN without solid surface contaminants such as carbon.[51,52]

To date, TiN structures formed by coating preexisting scaffolds with PEALD have been relatively large (>250 nm),[7,38,39,42,49] and PEALD work has not focused on exploiting the control over optical and electronic properties afforded by localized surface plasmonic resonances (LSPRs). LSPRs in small metallic nanostructures enable resonantly enhanced optical absorbance of light at specific frequencies.[53] LSPRs can also generate hot electrons that can be injected into the conduction band of an insulator or semiconductor[54–57] to produce sub-bandgap photocurrent.[54,58,59] Plasmonic absorption is a powerful tool for increasing photogeneration in metal-semiconductor devices; photodetectors and photovoltaic devices that exploit LSPRs in nanostructured TiN have been reported.[8,60–62]

In this work, we explore the infilling of the voids in ZnO NC networks with TiN via PEALD to produce plasmonic ZnO-TiN nanocomposites exhibiting LSPRs. While PEALD's ability to conformally coat larger structures with crystalline TiN at low temperature is known, it is *a priori* not clear that this will also apply to networks of NCs because some of the reactive species produced by a plasma are short-lived and deposition in the network may depend on the competition among surface reactivity, recombination, and diffusion.[63] Here, we demonstrate the formation of TiN throughout a 300 nm thick tortuous ZnO NC network. The as-produced films are plasmonic and contain crystalline TiN. By tuning the NC film thicknesses, PEALD parameters, and the number of PEALD cycles, we optimize the plasmonic response of the ZnO-TiN nanocomposites. We use these plasmonic nanocomposite films to create devices based on hot carrier injection, which generate photocurrent at zero bias.

II. EXPERIMENT

A. ZnO NC film synthesis

ZnO NCs are synthesized in a nonthermal plasma reactor previously described[2,64] and are schematically shown in Fig. 1(a). The average ZnO NC diameter as measured by XRD and TEM for all films is 10 nm. NCs are accelerated through a slit orifice and inertially impacted onto glass slides.[65,66] Film thicknesses are estimated from the deposition rate of ZnO from this reactor onto the substrate per transit of the substrate underneath the ZnO nanoparticle beam. Prior to deposition, the substrates (boroaluminosilicate glass, Corning Eagle XG) are cleaned by 2 min of sonication in acetone followed by 2 min of sonication in isopropanol.

B. TiN PEALD

The ZnO NC films were loaded into a Fiji 200 Gen 2 PEALD system (UltraTech) and allowed to outgas for 30 min under vacuum (30 mTorr) at 270 °C prior to deposition. The entire reactor is wrapped with insulation and is heated to prevent condensation. Inside the reactor, the substrate sits on a heated metal disk that is heated to 270 °C. Subsequently, pumping continued using only a rough vacuum pump (200 mTorr) as Ar and N_2 were fed through the reactor at 130 and 50 SCCM, respectively, for 2.4 s. Following this preparation period, cycles of TDMAT pulses and nitrogen plasma separated by nitrogen purges were used to infill the NC film with TiN. A single cycle consisted of (1) a 0.4 s pulse of TDMAT (260 mTorr), (2) 30 s with 30 SCCM N_2 flow (200 mTorr), (3) a 5 s purge with 10 SCCM Ar flow and 50 SCCM of N_2 (30 mTorr), (4) a 40 s 300 W inductively coupled plasma dose with 10 SCCM Ar and 50 SCCM N_2 (30 mTorr), and (5) a 10 s purge with 10 SCCM Ar and 50 SCCM N_2 mixture (30 mTorr). The total number of cycles was varied.

C. Photodetector fabrication

First, a $1 \times 1\ cm^2$ (100) Si substrate was coated with 300 nm of Al using an MBraun thermal evaporator. Second, the Al was coated with TiN using 55 PEALD cycles (~5 nm). Third, a 10 nm layer of TiO_2 was grown on the TiN with ALD (Cambridge Nanotech/Ultratech Savannah S200 ALD system) at 180 °C using water and TDMAT. Fourth, ZnO NCs were deposited on the TiO_2 layer using a nonthermal plasma. Fifth, this ZnO NC film was infilled with 55 cycles of TiN PEALD to form the photoactive nanocomposite. Finally, 300 nm of Al was deposited on a small area in the corner of the nanocomposite film to form the top contact. The device surface area is roughly $1 \times 0.4\ cm^2$. A 40 W T4 xenon light source was used to illuminate devices. The power as measured at the devices location was a uniform 32 mW/cm^2. Each device was measured with this incident power. Detector photocurrent data in the associated Figures are normalized to this power. To collect photocurrent measurements, the device was

Published under license by AVS.

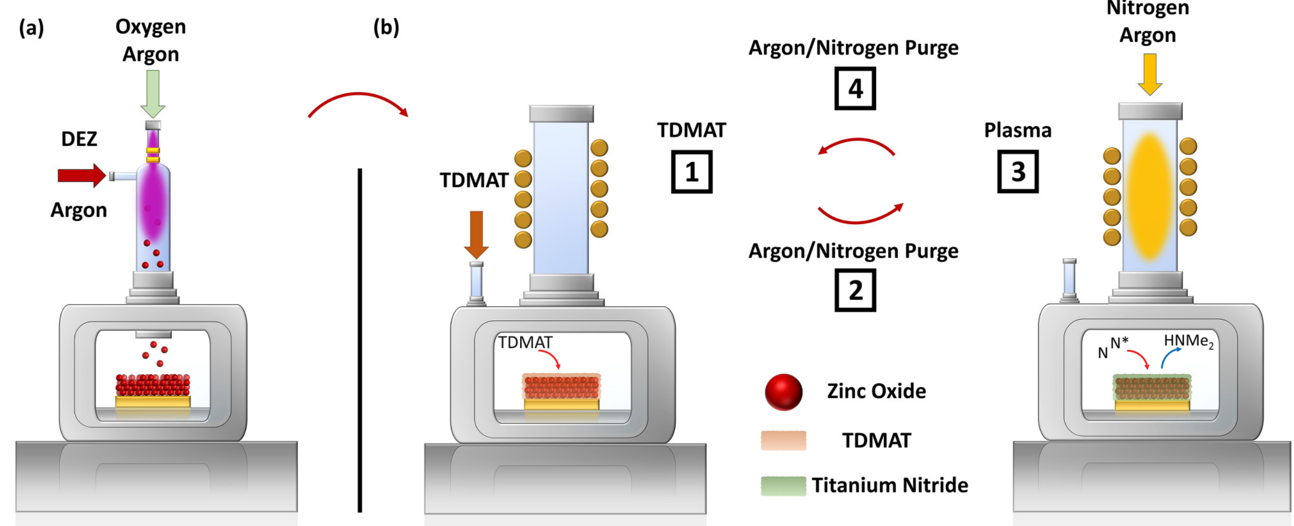

FIG. 1. ZnO-TiN nanocomposite synthesis. (a) ZnO NCs are synthesized in a nonthermal plasma using diethyl zinc, oxygen, and argon. The NCs are inertially impacted onto glass slides by accelerating the particle-laden gas flow through a slit orifice. (b) The NC films are infilled with TiN using multiple PEALD cycles, where a single cycle consists of a TDMAT pulse (1); argon purge (2); nitrogen plasma (3); and a final argon purge (4).

operated with 2 s of light exposure followed by 8 s of darkness [Figs. S7 and S8 (Ref. 114)].

D. Compositional and optical characterization

X-ray photoelectron spectroscopy (XPS, Phi VersaProbe III X-ray/ultraviolet photoelectron spectrometer) in conjunction with sputter depth profiling was used to study the chemical composition of the ZnO-TiN nanocomposite films. Composition spectra were collected at 280 eV bandpass energy while high resolution scans were taken at 55 eV bandpass energy for ten collection cycles. For depth profiling, the films were sputtered using 3 kV argon ions. Sputtering depths were estimated by sputtering to the bottom of the film and normalizing the estimated sputtering rate (9.7 nm/min for SiO_2 on Si) to the actual film thickness from that focused ion beam (FIB) section (~250 nm) to obtain an approximate depth during XPS collection. We note that the average film thickness measured by FIB-SEM for these films is 300 nm across several samples. UV-Vis spectroscopy (Agilent Cary 5000 spectrophotometer in the transmission mode) was used to measure plasmonic responses of the films.

E. Electron microscopy

Scanning transmission electron microscopy-energy dispersive x-ray spectroscopy (STEM-EDX) was used to measure the TiN infilling of the NC film and to characterize the structure of the photodetector samples. TEM cross-sectional lamellae were prepared using an FEI Helios NanoLab G4 dual-beam FIB and subsequently studied in an aberration-corrected FEI Titan G2 60-300 STEM equipped with a Super-X EDX spectrometer. When analyzing the ZnO-TiN nanocomposite films, the STEM was operated at 200 kV with a probe convergence angle of 25 mrad and a beam current of 120 pA. STEM-EDX maps were collected with 764 pixels by 764 pixels over a 400 by 400 nm area, a dwell time of 4 μs/pixel, and an acquisition time of 15 min with drift correction. When analyzing the photodetector, the STEM was operated at 60 kV and STEM-EDX maps were collected with 1024 pixels by 1024 pixels over 900 by 900 nm area; all other operating parameters were kept the same. Compositional maps from STEM-EDX data were made by integrating C, O, Si, Al, Ti, and Zn K-edge intensities after background subtraction. The Ga and Cu K and L-edges were omitted from the datasets shown. A three-pixel Gaussian blur was applied to the STEM-EDX maps to aid visualization. The elemental quantification was performed using the Bruker ESPRIT 1.9 software package.

F. Numerical modeling

Calculations to determine the effect of core-shell scattering were performed in python using a Mie scattering model, pymiecoated.[67] Values for the index of refraction and extinction coefficient of TiN (Ref. 68) and ZnO (Ref. 69) were used from the literature.

G. Spectroscopic ellipsometry

The complex index of refraction for each material was extracted from ellipsometric measurements on a J.A. Woollam variable-angle spectroscopic ellipsometer. Measurements were taken at incident angles between 55° and 75° over the wavelength range of 400–1100 nm. All samples were measured on backside-opacified glass substrates. The dense film of TiN was modeled as a single uniform layer while the ZnO particulate film was modeled as a composite bilayer that consists of a lower layer with varying thickness and a thin rough upper layer. The uppermost layer was

Published under license by AVS.

treated as a 50% by volume linear effective medium between the lower layer and air. The ZnO/TiN nanocomposite was modeled as a single uniform layer. Complex indices of refraction were fit point-by-point along with thicknesses to extract optical properties. The measured and modeled Ψand Δ for the TiN, ZnO, and ZnO/TiN films are reported in Figs. S1(a)–(c).[114] Extracted real and imaginary components of the indices of refraction for these materials are provided in Fig. S1(e).[114] Real (ε_1) and imaginary (ε_2) components of the material dielectric constants are shown in Fig. S1(f).[114] Additional modeling information is also available in the supplementary material.[114]

III. RESULTS AND DISCUSSION

A. Film characterization with XPS and EDX

It is *a priori* not obvious that PEALD should be capable of infilling the tortuous networks of NCs because there is no direct line of sight for plasma-generated species, such as nitrogen radicals, to reach the inner surfaces, particularly those near the substrate. Therefore, we investigated the depth variation of TiN deposition using STEM-EDX. STEM-EDX mapping of cross sections produced via FIB [Figs. 2(a) and 2(b)] shows that titanium and nitrogen are found throughout the film, demonstrating that PEALD can deposit TiN onto NC surfaces in pores at least 300 nm below the film's surface. The varying concentration of Ti and N throughout the sample is due to a combination of both uneven compaction of the ZnO NC film and the attenuation of nitrogen penetration at greater depths, as discussed below. The STEM-EDX results are corroborated by XPS and are shown in Fig. 2(c). XPS utilizes a spatially averaged result from a larger surface area of the film than the STEM-EDX. The uneven compaction of the ZnO NC film results in an NC film that is denser at the bottom than at the top; this is shown as an increase in the ZnO compositional fraction. The nitrogen attenuation results in the subsequent nitrogen fraction decrease through the film.

High-energy-resolution XPS scans provide further information about the bonding configuration of Ti in the film. The Ti 2p peak was fitted using four sets of doublets that correspond to TiO_2, TiON, TiN, and TiC. Doublet peak distances between TiN, 5.9 eV,[70] and TiO_2, 5.8 eV,[71,72] were fixed before fitting TiC and TiON peaks. Due to the Coster–Kronig effect, XPS peak widths are broader than usual.[73–75] Also, to account for inelastic scattering, the doublet area ratio was allowed to deviate from 1:2 for the TiON and TiO_2 peaks;[21,75] the TiN 1:2 area ratio was always satisfied. All peaks were shifted according to an adventitious carbon peak at 284.8 eV, although slight discrepancies in that value have been reported for adventitious carbon on TiN films.[76] In the XPS spectra, the Ti $2p_{3/2}$ level exhibits four distinct sets of peaks that change in area throughout the film and correspond to TiN, TiON, TiO_2, and TiC. The TiN peaks are located at 454.4, 454.7, 455.0, and 455.1 eV;[77–84] the TiO_xN_y peaks at 455.9, 456.2, 456.4, and 456.6 eV;[83,85] the TiO_2 peaks at 457.9, 458.0, 458.3, and 458.4 eV,[83,84,86,87] and the TiC set of peaks are located at 454.2, 453.9, 454.4, and 454.5 eV.[88–90] To investigate possible changes in the other elements, scans of Zn, O, N, and C are provided in Fig. S2.[114] Nitrogen bonding at 396 and 397 eV are attributed to two types of bonding, Ti—N—Ti and Ti—N—O;[91–93] however, other authors have reported that the peak at 396 eV could also refer to a β—N phase.[81,94] Peaks at 400 eV correspond to Ti—O—N bonding,[92,93] and the peak at 402 eV corresponds to chemisorbed γ—N_2.[93,95] O locations at 530 eV are consistent with TiO_2 (Ref. 96) and ZnO (Ref. 97), and peaks at 531 eV correspond to Ti—O—N,[96] Ti—OH, and Zn—OH.[98] C peaks at 284.8 eV correspond to C—C,[96] 286 eV to C—O,[96] and 288 eV to O=C—O.[96] Finally, the Zn peaks at 1021 and 1023 correspond to Zn—O and Zn—OH.[97,98]

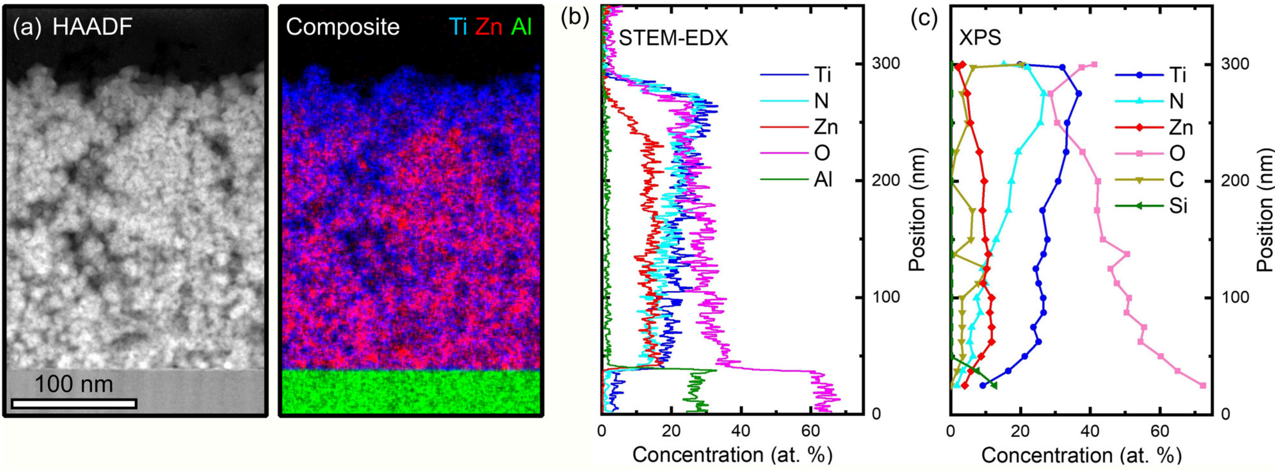

FIG. 2. Compositional analysis of a 300 nm ZnO-TiN nanocomposite film deposited on a sapphire substrate. (a) High Angle Annular Dark Field (HAADF)-STEM image and composite STEM-EDX map of a cross-sectional FIB lamella, showing the structure of the film and the distribution of Ti, Zn, and Al in the sample. (b) The concentration profile of Ti, N, Zn, O, and Al in the region shown in (a). (c) Depth profile of the same film using XPS.

Published under license by AVS.

B. TiN deposition mechanisms

Based on the EDX and XPS results in Figs. 2 and 3, we propose the following reaction mechanism for the TiN PEALD process. Initially, the surface of the plasma-synthesized ZnO NCs are terminated with surface hydroxyl groups.[1] During the initial TDMAT pulse, TDMAT reacts with these surface hydroxyl groups to yield a Ti—O—Zn bond similar to the Ti—O—Ru bonds formed during TDMAT deposition onto RuO_2.[99] The reaction should proceed with hydrogen from the surface reacting with an NMe_2 (H_3C—N—CH_3) group, which desorbs from the surface as $HNMe_2$.[51,52] TDMAT thermal decomposition does not occur at the temperatures used in this process.[51,52,100,101] Titanium is found throughout the film, which indicates that TDMAT (or one of its products) is capable of reaching the bottom of the ZnO NC film and reacting with the surface during the TDMAT pulse.

Nitrogen radicals created by dissociation of N_2 during the high-density inductive plasma step react with the surface bound titanium-amine compound. These radicals initiate nitrogen transamination reactions with the remaining NMe_2 on the surface to yield TiN as they diffuse through the network.[25] Nitrogen radical penetration into the film is limited both by reaction probability with a surface site and by recombination of nitrogen within the network.[63] These competing reactions inherently limit the penetration depth of the TiN; this competition is evidenced by the slight gradient of TiN through the network (Figs. 2 and 3) that is beginning to become apparent as the depth nears 300 nm. However, our results indicate that the nitrogen radical penetration depth limit is still greater than 300 nm, the thickness of the ZnO NC network.

To study the role of the N_2 plasma species that impinge on the surface of the ZnO nanoparticles that are not bonded to TDMAT or Ti during the first few cycles, three films exposed to 0, 10, and 55 PEALD cycles were produced using the same recipe as for TiN deposition, but the TDMAT step was replaced with Ar flow. In Fig. S3,[114] the Zn, O, and N peaks collected after 0, 10, and 55 cycles of plasma exposure reveal that a small number of N molecules bonded to the surface of the ZnO NCs as Zn—O—N.[97] Films contained less than 2% nitrogen after ten cycles; hence, it was difficult to collect any significant signal from a nitrogen scan. Differences in Zn and O peaks in XPS were not present from the control experiment of 0 cycles. From these experiments, it appears unlikely that that the nitrogen plasma significantly modifies the ZnO particles, as the particles will be increasingly covered with the TiN film that shields the underlying ZnO from nitrogen species.

We note that UV radiation from the plasma could be a contributor to TiN formation in the upper layers of the film as high-energy (>10 eV) photons are emitted from the discharge.[102] This radiation could ionize nitrogen in the first few NC layers of the film, but this process is highly unlikely to contribute to dissociation deep within the film due to the strong UV absorption of ZnO

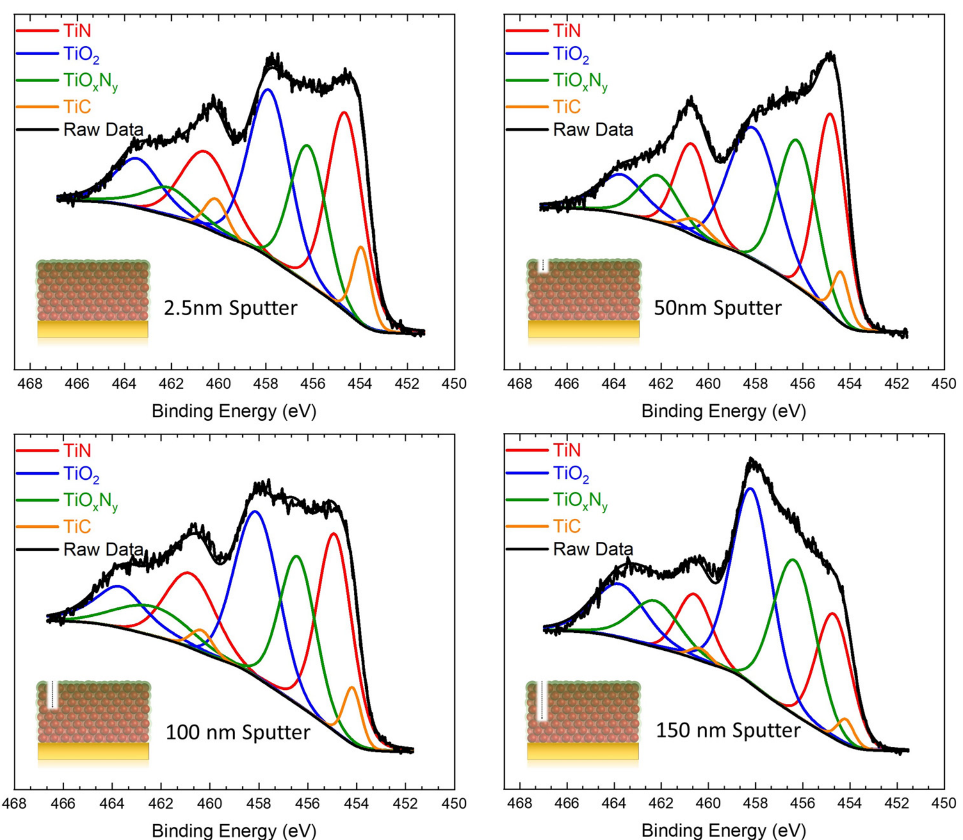

FIG. 3. XPS of a 300 nm ZnO NC film infilled with titanium nitride. Ti 2p peaks were fitted according to literature to determine the presence of TiO_2, TiN, TiC, and TiON. TiN can be found throughout the film as indicated by a 150 nm sputter.

Published under license by AVS.

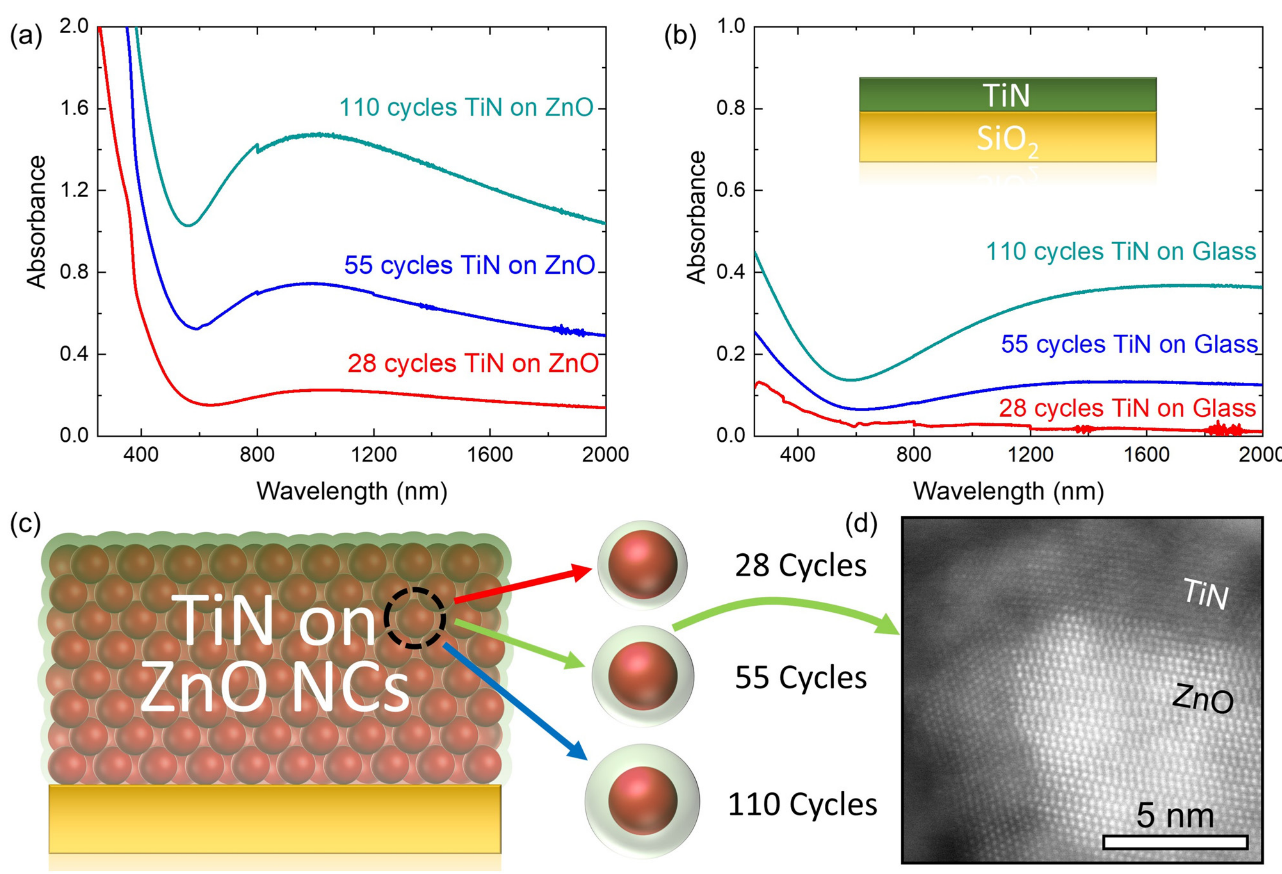

FIG. 4. Plasmonic and structural features of the ZnO-TiN nanocomposite. Note the different scales for (a) and (b). (a) UV-Vis spectra from a ZnO-TiN nanocomposite, with thicker coatings showing more absorbance and a more pronounced LSPR feature. (b) TiN coatings directly on glass. The UV-Vis absorption profiles indicate a thin film of TiN, growing with the number of PEALD cycles. (c) Schematic of the ZnO-TiN nanocomposite. (d) An atomic-resolution HAADF-STEM image of TiN (darker region) grown on a ZnO nanocrystal (brighter region) inside the NC network. This crystal was located ~20 nm from the top of the film in an FIB cross-sectional lamella.

[Fig. 4(a)]. Therefore, we suggest that the rate-limiting steps for TiN formation are nitrogen radical diffusion and nitrogen radical recombination/surface reactions throughout the network. This is also consistent with the higher fraction of TiO_2 found deeper in the film, which corresponds to TiO_2 at the interface of TiN and ZnO and TiO_2 that is found at the surface of the TiN in the network.

C. Plasmonic absorption of the ZnO-TiN nanocomposite

Figure 4 shows UV-Vis-IR absorption for TiN films deposited with different numbers of PEALD cycles on flat glass substrates and on ~300 nm thick ZnO NC networks. Assuming deposition similar to that on TiN PEALD directly on glass, each PEALD cycle deposits ~0.1 nm of TiN. Increasing the number of PEALD cycles resulted in an increase in the extinction, which we assume to be entirely due to absorption, of both the thin TiN films and the TiN infilled NC networks.[103,104] The TiN thin films show a broad surface plasmonic absorption feature peaking about ~1600 nm, whereas the ZnO-TiN nanocomposites show a pronounced LSPR at ~1000 nm which is blueshifted relative to the peak absorption of the TiN thin films. The extinction is also strongly enhanced compared to the thin-film samples; this is likely because the total quantity of TiN deposited on the ZnO NC network is larger than that on the flat substrate due to the high surface area within the NC network.[105] The LSPR peak wavelengths of our ZnO-TiN nanocomposites do not show a significant dependence on TiN layer thickness.

The LSPR absorption features of our ZnO-TiN nanocomposites are broader and redshifted compared to those in previous reports of LSPRs of TiN nanoparticles.[21,22] We attribute the broadness of the plasmonic peak to the morphological heterogeneity of the TiN in our NC networks as well as coated ZnO agglomerates that range in size. The TiN shells on the ZnO NCs are likely mixtures of TiN semishells[7] and close to full TiN shells[106] that have LSPRs with a range of peak wavelengths, and the absorption features we observe are composites of these various LSPR peaks. Moreover, the individual plasmonic elements are either connected

Published under license by AVS.

or are in close proximity to each other, leading to plasmonic coupling of adjacent shells, which also causes heterogeneity and a redshift of the LSPRs.[107,108]

Mie scattering calculations were performed to qualitatively understand the plasmonic properties of our nanocomposites. Nanoparticle films deposited by supersonic gas phase deposition are known to have a mesoscopic pore size distribution.[109] Such films can thus be envisioned as being comprised of dense agglomerates and less-dense "pores." To qualitatively understand the optical properties of the films, we modeled such agglomerates of ZnO particles after TiN deposition as spherical ZnO core:TiN shell particles, with ZnO core diameters on the order of several 10 nm. There is a range of coated ZnO agglomerate sizes that cumulatively produce these absorbance profiles, Fig. S4.[114] While previous studies of plasmonic nanoparticles have often observed only slight dependences of LSPR wavelengths on nanostructure with sizes of 10s of nanometers,[20,110,111] quite significant blueshifts are observed between TiN thin films and our nanocomposites, as shown by Figs. 4(a), 4(b), 5(a), and 5(b). The blueshift observed between thin-film samples and nanocomposites seems to be consistent with the concept of ZnO agglomerate cores covered with a TiN shell, as shown by Fig. S4.[114] In fact, the optical properties of our nanocomposites seem best approximated by a 75 nm ZnO core diameter with a shell thickness of around 3–4 nm, but this similarity should not be overinterpreted due to the approximated nature of our core-shell model. The increase in absorbance at low wavelengths <400 nm may be reflective of a size distribution of agglomerates but also of interband transitions.[112]

To investigate the effects of PEALD parameters on the TiN plasmonic response, the durations of the plasma exposure and purge times were varied. Based on EDX results, we concluded that TDMAT effectively penetrates the entire film, and therefore the influence of the TDMAT pulse time was not investigated. Figure 5(a) shows that increasing the duration of the plasma exposure (during which the films are exposed to nitrogen radicals) from 13 to 40 s increases the plasmonic absorption significantly. Tripling that time to 120 s resulted in little further increase in extinction suggesting that the influence of plasma exposure time effectively saturates between 13 and 40 s. As for purge times, significantly shorter times are required for saturation. The shortest purge times tested, 5 s after nitrogen plasma exposure and 10 s after TDMAT exposure instead of the typical 30 s purges, resulted in only a minimal change in LSPR peak absorbance (<0.1 absorbance unit) as shown in Fig. S5.[114] Due to the high flow of argon during the TDMAT pulse and the reduction in pressure during the purge step, it is unlikely that any TDMAT remains in the gas phase. Once the plasma is turned off, most of the remaining nitrogen radicals are expected to rapidly recombine, react with the film, or react with the surface of the reactor. Thus, 5 s after TDMAT and 10 s after the plasma pulse are long enough to remove the radicals from the chamber.

Figure 5(b) shows the plasmonic response of the film as a function of the ZnO NC film thickness. "0 nm ZnO" denotes TiN deposition on a flat glass substrate demonstrating absorption characteristics of a thin TiN film.[103,104] Thickness of these films are estimated from a known deposition rate of 10 nm per transit of the substrate under the ZnO nanocrystal beam. Increasing the ZnO NC film thickness up to 300 nm increases the plasmon absorption.

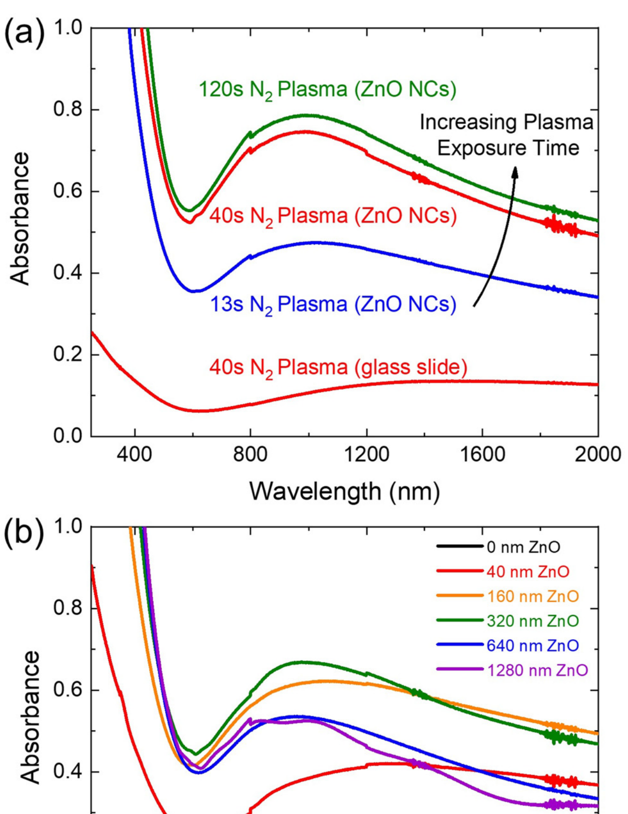

FIG. 5. Changes in the TiN plasmonic response when varying PEALD parameters and ZnO NC film thickness. (a) The effect of nitrogen plasma exposure time on the infilling quality as measured by UV-Vis of the films. (b) ZnO-TiN nanocomposite absorbance data based on the thickness of the initial ZnO NC coating.

Beyond 300 nm, a reduction in absorption is observed. We hypothesize that film porosity and nanocrystal impaction time are not linearly related such that very thin [Fig. S9 (Ref. 114)] and very thick networks are denser than the 300 nm film.[113] A denser film produced at longer deposition times would reduce our ability to deposit deep within the pores of the network and thus reduce the overall plasmonic response. However, further characterization of the morphology of the thicker aerosol-deposited ZnO films is required to determine the cause of this reduction in LSPR absorption.

D. Photodetector

A photodetector based on a 300 nm thick ZnO-TiN nanocomposite was fabricated using the conditions and process parameter

Published under license by AVS.

choices that maximized the LSPR intensity as discussed previously. The structural and compositional details of the photodetector are shown in Fig. 6. This device utilizes a potential barrier created by the metal-semiconductor or metal-insulator junction between TiN and either ZnO or TiO_2 and has the advantage of operating without bias (V = 0). This potential barrier limits current to flow to one direction.[57] Photocurrent can be generated by hot electrons generated by optical excitation in the metal entering the conduction band of the semiconductor[96] and/or by band to band transitions in ZnO and TiN excited by the white light source used. This concept of hot carrier injection has been demonstrated previously in conventional thin-film devices based on planar ZnO/TiN interfaces.[8]

The ZnO-TiN nanocomposite-based device was compared with a conventional thin-film device produced by depositing the same number of cycles of TiN directly on a TiO_2 coated substrate with no ZnO NCs [see HAADF-STEM in Fig. S6 (Ref. 114)]. As shown in Fig. 6(d), 300 nm of the ZnO-TiN nanocomposite were required to produce a higher photocurrent (0.12 μA/mW) compared to the planar TiN device (0.09 μA/mW). ZnO thicknesses of 10, 50, and 100 nm were also tested [see Fig. S7 (Ref. 114)] and produced less photocurrent than both the 0 and 300 nm cases. The 50 nm ZnO:TiN photodetector produced less average current (0.05 μA/mW) than the 100 nm ZnO:TiN device (0.06 μA/mW). The mean value and deviations of the photocurrent measurements are shown in Fig. S8.[114]

The nonmonotonic behavior of these devices and the overall plasmonic response might be due to denser ZnO NC networks reaching their TiN infill limits sooner than less-dense networks. After each cycle of PEALD of TiN, the porosity of the network decreases until the network becomes too dense to allow for continued transport of TDMAT or nitrogen radicals within the network eventually leading to the deposition on top of the film for the remainder of the cycles [see Fig. S9 (Ref. 114)]. The resulting film performance would be more akin to a TiN film on top of a thick ZnO film rather than an infilled NC network (Fig. 6), which would explain the decrease in conductivity compared to both a more

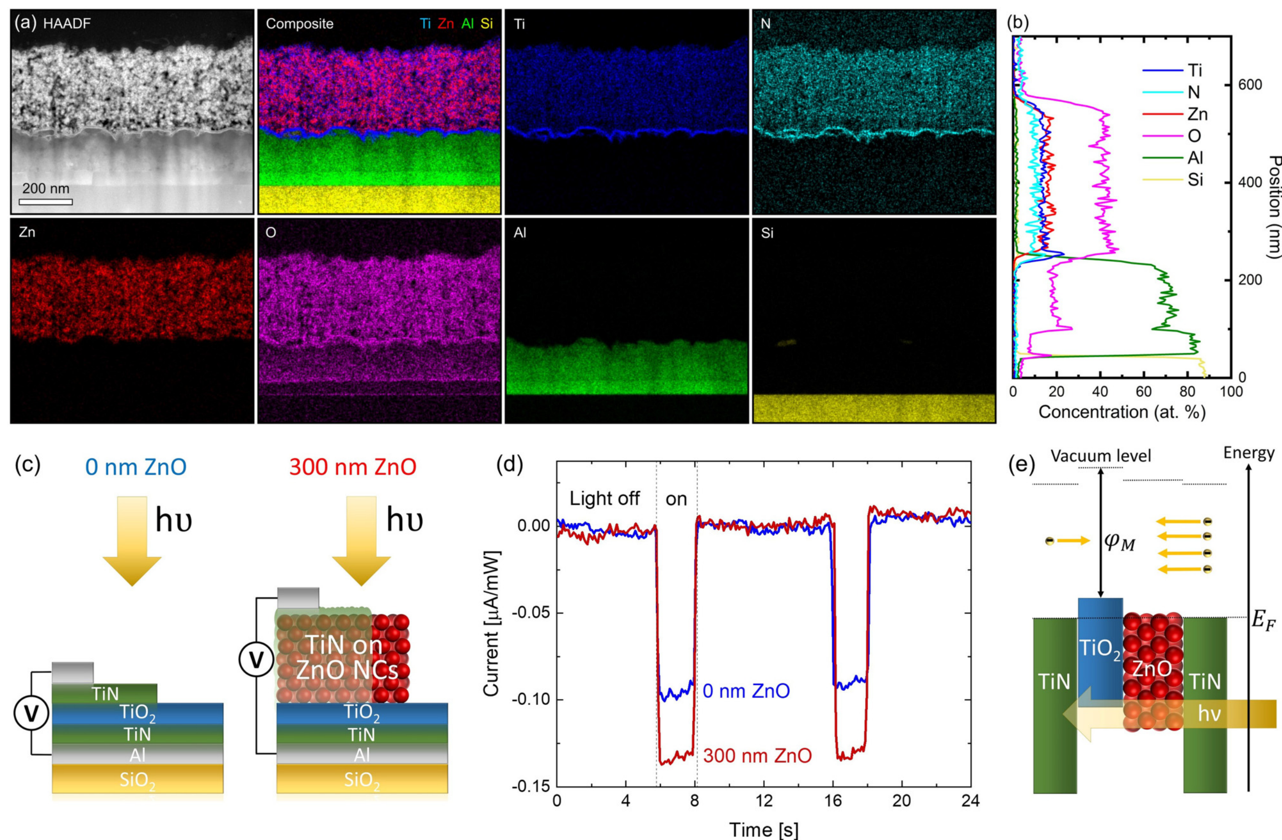

FIG. 6. ZnO-TiN nanocomposite photodetector. (a) HAADF-STEM image, composite STEM-EDX map, and individual EDX elemental maps of Ti, N, Zn, O, Al, and Si obtained from a cross-sectional FIB lamella of a 300 nm photodetector. (b) The concentration profiles of the elements shown in (a) over this region. The amount of TiN tapers slightly with increasing depth. (c) Schematics of the nanocomposite-based photodetector and conventional thin-film photodetector. (d) Photocurrent measurements of the nanocomposite-based photodetector (red, 300 nm ZnO) and conventional thin-film photodetector (blue, 0 nm ZnO). (e) Band diagram for the network, where φ_m is the work function of TiO_2 and E_F is the Fermi level energy.

Published under license by AVS.

porous ZnO network and also a planar film. This would also explain the failure to produce significant plasmonic absorption for these thinner films (see Fig. 5).

IV. CONCLUSION

ZnO-TiN nanocomposite films were produced by infilling ZnO NC networks with TiN using PEALD. Despite the tortuosity inside the NC networks, nitrogen radicals are capable of reaching the bottom of the networks to form TiN during the plasma step in the PEALD cycle even for NC networks as thick as 300 nm. The as-synthesized nanocomposite films exhibited plasmonic absorption in the near-infrared due to the nanostructured crystalline TiN. Maximizing the LSPR absorption required a 40 s nitrogen plasma exposure. Finally, the plasmonic nanocomposite was used to produce a photodetector requiring no bias voltage that required 300 nm in order to exhibit higher photocurrent than an analogous conventional thin-film device with no ZnO NCs.

ACKNOWLEDGMENTS

This project was supported by the MRSEC program of the National Science Foundation under Award No. DMR-1420013 and by the Research Experiences for Undergraduates (REU) Program of the National Science Foundation under Award No. DMR-1852044. STEM, XPS, and ellipsometry were performed in the College of Science and Engineering Characterization Facility of the University of Minnesota, which receives partial support from the NSF through the MRSEC program. Portions of this work were conducted in the Minnesota Nano Center, which is supported by the National Science Foundation through the National Nano Coordinated Infrastructure Network (Award No. NNCI-1542202). N.M.C. acknowledges support from the NSF Graduate Research Fellowship under Grant No. 00074041. The authors thank T. L. Senkow for her assistance in editing the manuscript. The authors are grateful to Ognjen Ilic for advice regarding the Mie scattering calculations.

REFERENCES

[1] B. L. Greenberg, Z. L. Robinson, K. V. Reich, C. Gorynski, B. N. Voigt, L. F. Francis, B. I. Shklovskii, E. S. Aydil, and U. R. Kortshagen, Nano Lett. **17**, 4634 (2017).
[2] E. Thimsen, M. Johnson, X. Zhang, A. J. Wagner, K. A. Mkhoyan, U. R. Kortshagen, and E. S. Aydil, Nat. Commun. **5**, 5822 (2014).
[3] B. L. Greenberg, Z. L. Robinson, Y. Ayino, J. T. Held, T. A. Peterson, K. A. Mkhoyan, V. S. Pribiag, E. S. Aydil, and U. R. Kortshagen, Sci. Adv. **5**, eaaw1462 (2019).
[4] Y. Liu, M. Gibbs, C. L. Perkins, J. Tolentino, M. H. Zarghami, J. Bustamante, and M. Law, Nano Lett. **11**, 5349 (2011).
[5] J. Y. Woo, J. Lee, H. Lee, N. Lee, J. H. Oh, Y. R. Do, and C.-S. Han, Opt. Express **21**, 12519 (2013).
[6] R. W. Crisp, F. S. M. Hashemi, J. Alkemade, N. Kirkwood, G. Grimaldi, S. Kinge, L. D. A. Siebbeles, J. R. Ommen, and A. J. Houtepen, Adv. Mater. Interfaces **7**, 1901600 (2020).
[7] M. B. Cortie, J. Giddings, and A. Dowd, Nanotechnology **21**, 115201 (2010).
[8] S. Ishii, S. L. Shinde, W. Jevasuwan, N. Fukata, and T. Nagao, ACS Photonics **3**, 1552 (2016).
[9] E. Ozbay, Science **311**, 189 (2006).
[10] E. B. Dickerson, E. C. Dreaden, X. Huang, I. H. El-Sayed, H. Chu, S. Pushpanketh, J. F. McDonald, and M. A. El-Sayed, Cancer Lett. **269**, 57 (2008).
[11] S. Schelm and G. B. Smith, Appl. Phys. Lett. **82**, 4346 (2003).
[12] M. S. Shishodia and P. Pathania, Phys. Plasmas **25**, 042101 (2018).
[13] Z. Xie, X. Liu, W. Wang, C. Liu, Z. Li, and Z. Zhang, Nanoscale Res. Lett. **9**, 1 (2014).
[14] N. Kinsey, M. Ferrera, G. V. Naik, V. E. Babicheva, V. M. Shalaev, and A. Boltasseva, Opt. Express **22**, 12238 (2014).
[15] H. C. Chen, B. H. Tseng, M. P. Houng, and Y. H. Wang, Thin Solid Films **445**, 112 (2003).
[16] Z. Xie, X. Liu, P. Zhan, W. Wang, and Z. Zhang, AIP Adv. **3**, 062129 (2013).
[17] X. Y. Zhang, P. Song, and X. L. Cui, J. Adv. Oxid. Technol. **16**, 131 (2013).
[18] T. Takata, C. Pan, and K. Domen, Sci. Technol. Adv. Mater. **16**, 033506 (2015).
[19] U. Guler *et al.*, Adv. Opt. Mater. **5**, 1600717 (2017).
[20] U. Guler, S. Suslov, A. V. Kildishev, A. Boltasseva, and V. M. Shalaev, Nanophotonics **4**, 269 (2015).
[21] K. S. Schramke, Y. Qin, J. T. Held, K. A. Mkhoyan, and U. R. Kortshagen, ACS Appl. Nano Mater. **1**, 2869 (2018).
[22] A. Alvarez Barragan, N. V. Ilawe, L. Zhong, B. M. Wong, and L. Mangolini, J. Phys. Chem. C **121**, 2316 (2017).
[23] O. Sánchez, M. Hernández-Vélez, D. Navas, M. A. Auger, J. L. Baldonedo, R. Sanz, K. R. Pirota, and M. Vázquez, Thin Solid Films **495**, 149 (2006).
[24] I. R. Howell, B. Giroire, A. Garcia, S. Li, C. Aymonier, and J. J. Watkins, J. Mater. Chem. C **6**, 1399 (2018).
[25] A. Weber, R. Nikulski, C. P. Klages, M. E. Gross, R. M. Charatan, R. L. Opilan, and W. L. Brown, Appl. Surf. Sci. **91**, 314 (1995).
[26] C. J. Brennan, C. M. Neumann, and S. A. Vitale, J. Appl. Phys. **118**, 045307 (2015).
[27] M. Drygaś, C. Czosnek, R. T. Paine, and J. F. Janik, Chem. Mater. **18**, 3122 (2006).
[28] Z. Jiang and W. E. Rhine, Chem. Mater. **3**, 1132 (1991).
[29] M. K. S. Barr, L. Assaud, Y. Wu, C. Laffon, P. Parent, J. Bachmann, and L. Santinacci, Electrochim. Acta **179**, 504 (2015).
[30] M. Kulmas *et al.*, Adv. Funct. Mater. **26**, 4882 (2016).
[31] I.-S. Yu, H.-E. Cheng, C.-C. Chang, Y.-W. Lin, H.-T. Chen, Y.-C. Wang, and Z.-P. Yang, Opt. Mater. Express **7**, 777 (2017).
[32] M. Q. Snyder, S. A. Trebukhova, B. Ravdel, M. C. Wheeler, J. DiCarlo, C. P. Tripp, and W. J. DeSisto, J. Power Sources **165**, 379 (2007).
[33] M. Ritala, M. Leskelä, J. Dekker, C. Mutsaers, P. J. Soininen, and J. Skarp, Chem. Vap. Deposition **5**, 7 (1999).
[34] G. K. Hyde, S. D. McCullen, S. Jeon, S. M. Stewart, H. Jeon, E. G. Loboa, and G. N. Parsons, Biomed. Mater. **4**, 025001 (2009).
[35] P. Banerjee, I. Perez, L. Henn-Lecordier, S. B. Lee, and G. W. Rubloff, Nat. Nanotechnol. **4**, 292 (2009).
[36] J. Musschoot, Q. Xie, D. Deduytsche, S. Van den Berghe, R. L. Van Meirhaeghe, and C. Detavernier, Microelectron. Eng. **86**, 72 (2009).
[37] Y. J. Lee, Mater. Lett. **59**, 615 (2005).
[38] L. Assaud, K. Pitzschel, M. Hanbucken, and L. Santinacci, ECS J. Solid State Sci. Technol. **3**, P253 (2014).
[39] J. Y. Kim, D. Y. Kim, H. O. Park, and H. Jeon, J. Electrochem. Soc. **152**, G29 (2005).
[40] D. Longrie, D. Deduytsche, J. Haemers, P. F. Smet, K. Driesen, and C. Detavernier, ACS Appl. Mater. Interfaces **6**, 7316 (2014).
[41] I. Krylov, E. Zoubenko, K. Weinfeld, Y. Kauffmann, X. Xu, D. Ritter, and M. Eizenberg, J. Vac. Sci. Technol. A **36**, 51505 (2018).
[42] E. Kao, C. Yang, R. Warren, A. Kozinda, and L. Lin, Sens. Actuators A Phys. **240**, 160 (2016).
[43] M. Burke *et al.*, J. Vac. Sci. Technol. A **33**, 01A103 (2015).
[44] M. Burke, A. Blake, I. M. Povey, M. Schmidt, N. Petkov, P. Carolan, and A. J. Quinn, J. Vac. Sci. Technol. A **32**, 031506 (2014).
[45] P. Caubet *et al.*, J. Electrochem. Soc. **155**, H625 (2008).

Published under license by AVS.

[46]N. Samal, H. Du, R. Luberoff, K. Chetry, R. Bubber, A. Hayes, and A. Devasahayam, J. Vac. Sci. Technol. A **31**, 01A137 (2013).
[47]D.-H. Kim, Y. J. Kim, J.-H. Park, and J. H. Kim, Mater. Sci. Eng. C **24**, 289 (2004).
[48]J. Härkönen *et al.*, Nucl. Instrum. Methods Phys. Res. Sect. A **831**, 2 (2016).
[49]E. Shkondin, T. Repän, O. Takayama, and A. V. Lavrinenko, Opt. Mater. Express **7**, 4171 (2017).
[50]S. B. S. Heil, J. L. van Hemmen, C. J. Hodson, N. Singh, J. H. Klootwijk, F. Roozeboom, M. C. M. van de Sanden, and W. M. M. Kessels, J. Vac. Sci. Technol. A **25**, 1357 (2007).
[51]E. T. Norton and C. Amato-Wierda, Chem. Mater. **13**, 4655 (2001).
[52]J.-Y. Yun, J. Electrochem. Soc. **146**, 1804 (1999).
[53]H. Paul and R. Fischer, Am. J. Phys. **51**, 327 (1983).
[54]A. M. Brown, R. Sundararaman, P. Narang, W. A. Goddard, and H. A. Atwater, ACS Nano **10**, 957 (2016).
[55]A. Furube, L. Du, K. Hara, R. Katoh, and M. Tachiya, J. Am. Chem. Soc. **129**, 14852 (2007).
[56]C. G. Silva, R. Juárez, T. Marino, R. Molinari, and H. García, J. Am. Chem. Soc. **133**, 595 (2011).
[57]F. Wang and N. A. Melosh, Nat. Commun. **4**, 1711 (2013).
[58]J. A. Huang and L. B. Luo, Adv. Opt. Mater. **6**, 1701282 (2018).
[59]C. Clavero, Nat. Photonics **8**, 95 (2014).
[60]A. A. Hussain, B. Sharma, T. Barman, and A. R. Pal, ACS Appl. Mater. Interfaces **8**, 4258 (2016).
[61]D. M. Schaadt, B. Feng, and E. T. Yu, Appl. Phys. Lett. **86**, 063106 (2005).
[62]H. Wang, Q. Chen, L. Wen, S. Song, X. Hu, and G. Xu, Photonics Res. **3**, 329 (2015).
[63]H. C. M. Knoops, E. Langereis, M. C. M. van de Sanden, and W. M. M. Kessels, J. Electrochem. Soc. **157**, G241 (2010).
[64]B. L. Greenberg, S. Ganguly, J. T. Held, N. J. Kramer, K. A. Mkhoyan, E. S. Aydil, and U. R. Kortshagen, Nano Lett. **15**, 8162 (2015).
[65]N. P. Rao, N. Tymiak, J. Blum, A. Neuman, H. J. Lee, S. L. Girshick, P. H. McMurry, and J. Heberlein, J. Aerosol Sci. **29**, 707 (1998).
[66]Z. C. Holman and U. R. Kortshagen, Nanotechnology **21**, 335302 (2010).
[67]J. Leinonen, see https://github.com/jleinonen/pymiecoa for Mie scattering python code.
[68]J. Pflüger and J. Fink, in *Handbook of Optical Constants of Solids* (Academic, San Diego, 1997), Vol. 2, p. 293.
[69]W. L. Bond, J. Appl. Phys. **36**, 1674 (1965).
[70]D. Jaeger and J. Patscheider, Surf. Sci. Spectra **20**, 1 (2013).
[71]B. Bharti, S. Kumar, H.-N. Lee, and R. Kumar, Sci. Rep. **6**, 32355 (2016).
[72]R. Sanjinés, H. Tang, H. Berger, F. Gozzo, G. Margaritondo, and F. Lévy, J. Appl. Phys. **75**, 2945 (1994).
[73]R. Nyholm, N. Martensson, A. Lebuglet, and U. Axelsson, J. Phys. F Met. Phys. **11**, 1727 (1981).
[74]W. Bambynek, B. Crasemann, R. W. Fink, H. U. Freund, H. Mark, C. D. Swift, R. E. Price, and P. V. Rao, Rev. Mod. Phys. **44**, 716 (1972).
[75]K. S. Robinson and P. M. A. Sherwood, Surf. Interface Anal. **6**, 261 (1984).
[76]G. Greczynski and L. Hultman, ChemPhysChem **18**, 1507 (2017).
[77]L. Porte, L. Roux, and J. Hanus, Phys. Rev. B **28**, 3214 (1983).
[78]M. Repeta, L. Dignard-Bailey, J. F. Currie, J. L. Brebner, and K. Barla, J. Appl. Phys. **63**, 2796 (1988).
[79]H. Höchst, R. D. Bringans, P. Steiner, and T. Wolf, Phys. Rev. B **25**, 7183 (1982).
[80]A. Ermolieff, P. Bernard, S. Marthon, and P. Wittmer, Surf. Interface Anal. **11**, 563 (1988).
[81]N. C. Saha and H. G. Tompkins, J. Appl. Phys. **72**, 3072 (1992).
[82]B. Subramanian, C. V. Muraleedharan, R. Ananthakumar, and M. Jayachandran, Surf. Coat. Technol. **205**, 5014 (2011).
[83]Y. Han, X. Yue, Y. Jin, X. Huang, and P. K. Shen, J. Mater. Chem. A **4**, 3673 (2016).
[84]M. J. Vasile, J. Vac. Sci. Technol. A **8**, 99 (1990).
[85]M.-P. Delplancke-Ogletree and O. R. Monteiro, J. Vac. Sci. Technol. A **15**, 1943 (1997).
[86]C. Ernsberger, J. Nickerson, A. E. Miller, and J. Moulder, J. Vac. Sci. Technol. A **3**, 2415 (1985).
[87]M. V. Kuznetsov, J. F. Zhuravlev, and V. A. Gubanov, J. Electron Spectrosc. Relat. Phenom. **58**, 169 (1992).
[88]L. Zhang and R. V. Koka, Mater. Chem. Phys. **57**, 23 (1998).
[89]G. S. Girolami, J. A. Jensen, D. M. Pollina, C. M. Allocca, A. E. Kaloyeros, and W. S. Williams, J. Am. Chem. Soc. **109**, 1579 (1987).
[90]A. A. Galuska, J. C. Uht, and N. Marquez, J. Vac. Sci. Technol. A **6**, 110 (1988).
[91]Z. Zhou and Y. Huang, J. Phys. Conf. Ser. **188**, 012033 (2009).
[92]S. Oktay, Z. Kahraman, M. Urgen, and K. Kazmanli, Appl. Surf. Sci. **328**, 255 (2015).
[93]A. H. Alshehri, N. Nelson-Fitzpatrick, K. H. Ibrahim, K. Mistry, M. Yavuz, and K. P. Musselman, J. Vac. Sci. Technol. A **36**, 031602 (2018).
[94]A. Achour, R. L. Porto, M. A. Soussou, M. Islam, M. Boujtita, K. A. Aissa, L. Le Brizoual, A. Djouadi, and T. Brousse, J. Power Sources **300**, 525 (2015).
[95]N. D. Shinn and K.-L. Tsang, J. Vac. Sci. Technol. A **9**, 1558 (1991).
[96]G. Zorn, V. Migonney, and D. G. Castner, Biointerphases **9**, 031001 (2014).
[97]M. B. Haider, Nanoscale Res. Lett. **12**, 5 (2017).
[98]N. Mintcheva, A. Aljulaih, W. Wunderlich, S. Kulinich, and S. Iwamori, Materials **11**, 1127 (2018).
[99]A. Chaker, P. D. Szkutnik, J. Pointet, P. Gonon, C. Vallée, and A. Bsiesy, J. Appl. Phys. **120**, 085315 (2016).
[100]J. P. A. M. Driessen, J. Schoonman, and K. F. Jensen, J. Electrochem. Soc. **148**, G178 (2001).
[101]K. Sen, T. Banu, T. Debnath, D. Ghosh, and A. K. Das, Dalton Trans. **43**, 8877 (2014).
[102]U. Fantz, S. Briefi, D. Rauner, and D. Wünderlich, Plasma Sources Sci. Technol. **25**, 045006 (2016).
[103]A. Banerjee, R. M. Heath, D. Morozov, D. Hemakumara, U. Nasti, I. Thayne, and R. H. Hadfield, Opt. Mater. Express **8**, 2072 (2018).
[104]F. Chen, S.-W. Wang, L. Yu, X. Chen, and W. Lu, Opt. Mater. Express **4**, 1833 (2014).
[105]P. Mulvaney, Langmuir **12**, 788 (1996).
[106]S. Link and M. A. El-Sayed, J. Phys. Chem. B **103**, 4212 (1999).
[107]L. G. U. Kreibig, Surf. Sci. **156**, 678 (1985).
[108]H. Lange, B. H. Juárez, A. Carl, M. Richter, N. G. Bastús, H. Weller, C. Thomsen, R. Von Klitzing, and A. Knorr, Langmuir **28**, 8862 (2012).
[109]N. Vulic, J. V. Carpenter, P. Firth, N. Rodkey, Z. C. Holman, and S. M. Goodnick, ACS Appl. Energy Mater. **2**, 8587 (2019).
[110]M. J. Hostetler *et al.*, Langmuir **14**, 17 (1998).
[111]M. M. Alvarez, J. T. Khoury, T. G. Schaaff, M. N. Shafigullin, I. Vezmar, and R. L. Whetten, J. Phys. Chem. B **101**, 3706 (1997).
[112]A. Reinholdt, R. Pecenka, A. Pinchuk, S. Runte, A. L. Stepanov, T. E. Weirich, and U. Kreibig, Eur. Phys. J. D **31**, 69 (2004).
[113]S. Ghosh, X. Chen, C. Li, B. A. Olson, and C. J. Hogan, AIChE J. **66**, e16874 (2019).
[114]See supplementary material at https://doi.org/10.1116/1.5142858 for high resolution XPS of all elements; Mie theory core shell scattering and absorption simulation data; ellipsometry of TiN, ZnO, and ZnO-TiN; electrical measurements for all devices; STEM-EDX images of device produced without ZnO NCs; and the effect of purge times after TDMAT and after nitrogen plasma. This material is available free of charge via the Internet at http://pubs.acs.org.

Published under license by AVS.